ACS MATERIALS Au
AN OPEN ACCESS JOURNAL OF THE AMERICAN CHEMICAL SOCIETY

pubs.acs.org/materialsau

Article

Identification of Nanoscale Processes Associated with the Disorder-to-Order Transformation of Carbon-Supported Alloy Nanoparticles

Hannah M. Ashberry, Xun Zhan, and Sara E. Skrabalak*

Cite This: *ACS Mater. Au* 2022, 2, 143−153

Read Online

ACCESS | Metrics & More | Article Recommendations | Supporting Information

ABSTRACT: Due to their ordered crystal structures and high structural stabilities, intermetallic nanoparticles often display enhanced catalytic, magnetic, and optical properties compared to their random alloy counterparts. Intermetallic nanoparticles can be achieved by thermal annealing of their disordered (random alloy) counterparts. However, high temperatures and long annealing times needed to achieve the disorder-to-order transition often lead to a loss of sample monodispersity and an increase in the average size of nanoparticles. Here, we performed ex situ powder X-ray diffraction (XRD) and in situ annealing transmission electron microscopy (TEM) experiments to elucidate nanoscale processes that contribute to the ordering of carbon-supported PdCu nanoparticles as a model system. Random alloy PdCu nanoparticles supported on carbon were thermally annealed for various lengths of time at the disorder-to-order phase transition temperature, where changes in nanoparticle size and the crystal phase were monitored. The nanoparticles were only completely transformed to the intermetallic phase by undertaking measures to deliberately increase their size by increasing the number of nanoparticles on the carbon support. In situ annealing TEM experiments reveal nanoscale processes that account for the disorder-to-order phase transformation. Five different processes were observed at 400 °C. Isolated nanoparticles remained in the random alloy phase or underwent a phase transformation to the intermetallic phase. Nanoparticles fused with neighboring nanoparticles resulting in no change in phase or conversion to the intermetallic phase. Evidence of vapor transport was also observed, as some isolated nanoparticles were found to diminish in size upon heating. These variable processes account for the heterogeneity often observed for intermetallic nanoparticle samples achieved through annealing and motivate the development of synthetic routes that suppress particle−particle coalescence, as well as investigating metal−support interactions to facilitate the disorder-to-order phase transformation under mild conditions. Overall, this work furthers our knowledge of the formation of intermetallic nanoparticles by thermal annealing approaches, which could accelerate the development of electrocatalysts and the application of intermetallic nanoparticles in magnetic storage devices.

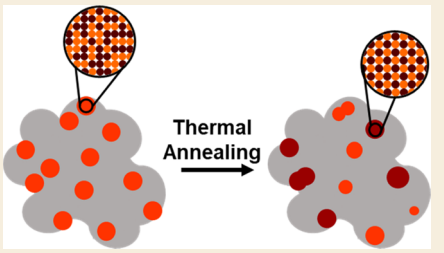

KEYWORDS: *in situ TEM, phase transitions, intermetallic, nanoparticles, catalysts*

INTRODUCTION

Intermetallic nanoparticles often exhibit remarkable catalytic, magnetic, and optical properties due to their long-range atomic ordering and defined stoichiometry.[1−6] For example, assemblies of random alloy FePt nanoparticles transformed to ferromagnetic assemblies upon conversion of FePt nanoparticles to the intermetallic phase; the ferromagnetic assemblies were chemically and mechanically robust and could support high-density magnetization applications.[7] Also, intermetallic Pt_3Co nanoparticles showed increased mass activity and durability for the oxygen reduction reaction (ORR) when compared to their random alloy counterpart.[8] Thermal annealing of preformed nanoparticles of the disordered phase in the atmosphere (or vacuum) is one method to attain intermetallic nanoparticles. In this two-step process, random alloy nanoparticles are synthesized and heated at high temperatures (≥500 °C) to induce the disorder-to-order phase transformation. Often these random alloy nanoparticles are added to support for thermal processing. Unfortunately, the high temperatures and long annealing times required to achieve the disorder-to-order transition are accompanied by an increase in nanoparticle polydispersity. Other routes can be taken to prevent polydispersity, such as encapsulating nanoparticles in a silica shell or using different types of nanoparticle supports that prevent sintering.[9,10] Here, we identify nanoscale processes that occur during the disorder-to-order transition of supported alloy nanoparticles, providing insight into how this polydispersity arises and may be mitigated.

In situ heating transmission electron microscopy (TEM) is well-suited for such studies, allowing for real-time observation of morphological and crystal structure changes during annealing. For example, Xiong and co-workers heated

Received: October 16, 2021
Revised: November 17, 2021
Accepted: November 19, 2021
Published: December 6, 2021

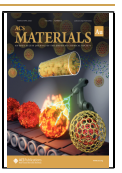

https://doi.org/10.1021/acsmaterialsau.1c00063
ACS Mater. Au 2022, 2, 143−153

carbon-supported random alloy Pt_3Co nanoparticles for 2 h at 750 °C and observed coarsening of nanoparticles with scanning transmission electron microscopy (STEM).[11] The primary coarsening process was observed to be particle coalescence, with nanoparticles migrating across the carbon support to collide and coalesce with neighboring nanoparticles.[11] After annealing, the number of smaller nanoparticles was decreased, while there was an increase in the number of larger nanoparticles, consistent with coarsening by particle coalescence.[11] Yao and co-workers used in situ heating STEM to reveal how surface composition played a role in the mobility and coalescence process with carbon-supported low-Pt-content alloy catalysts ($PtFe_3$, $PtCo_3$, and $PtNi_3$).[12] Nanoparticles with surface enrichment of the less-noble metal were associated with higher mobility on the carbon support and faster nanoparticle coalescence.[12] These studies provide excellent insight into the mobility and coalescence of random alloy nanoparticles during annealing; however, these events were not correlated to changes in the crystal structure of nanoparticles.

To address this gap in knowledge, we used ex situ powder X-ray diffraction (XRD) and in situ annealing TEM experiments to investigate particle coalescence events in conjunction with crystal structure changes. Carbon-supported random alloy PdCu nanoparticles were selected as a model system as our prior research revealed that the thermal annealing of carbon-supported PdCu nanoparticles led to the conversion to the intermetallic phase; however, there was a loss of monodispersity and an increase in the average size of the nanoparticles.[13] That is, the random alloy A1 phase of PdCu is converted to the intermetallic B2 phase, which belongs to the *Pm*3*m* space group, also known as the CsCl-type structure. The conversion to the intermetallic phase for PdCu nanoparticles is valuable in catalytic applications, where intermetallic nanoparticles have been shown to have increased catalytic activity and durability.[13−16] Often high temperatures and long annealing times are required to convert carbon-supported random alloy PdCu nanoparticles to their intermetallic counterpart, which results in sintering and loss of monodispersity.[3] Yet, studies are needed to identify the processes that occur during thermal annealing to help develop pathways to monodisperse samples in the future.

At the disorder-to-order phase transition temperature, these nanoparticles were thermally annealed for varying lengths of time, and changes in the size of the nanoparticles and crystal phase were monitored. Complete conversion to the intermetallic phase was only realized when the number of nanoparticles on the carbon support was increased in a deliberate attempt to increase the size of the nanoparticle via increased coalescence events. In situ annealing TEM experiments revealed five processes during annealing. This work ultimately is a call for synthetic routes for intermetallic nanoparticles that suppress particle−particle coalescence.

EXPERIMENTAL METHODS

Chemicals

Oleylamine (70%, OLA), palladium(II) acetylacetonate ($Pd(acac)_2$, 99%), and copper(II) acetylacetonate ($Cu(acac)_2$, 99%) were purchased from Millipore Sigma and unaltered.

Preparation of PdCu Random Alloy Nanoparticles

PdCu nanoparticles were synthesized by a modified procedure by Guo and co-workers.[17] To a 100 mL round-bottom flask (RBF) 20.0 mL of OLA was added and heated to 200 °C under Ar gas flow while stirring at 200 rpm. In a glass scintillation via, 60.9 mg of $Pd(acac)_2$, 52.3 mg of $Cu(acac)_2$, and 5 mL of OLA were heated at 80 °C with stirring at 1600 rpm until all of the metal precursors dissolved. The OLA and metal precursor solution was added dropwise (1 drop/s) to the RBF. The temperature was held at 200 °C for 1.5 h under Ar. The solution was cooled to 70 °C and approximately 6 mL of the resulting solution was added to four centrifuge tubes. The centrifuge tubes were filled to the 20 mL line with hexanes and centrifuged at 3900 rpm for 10 min to remove any large nanoparticles. The resulting supernatant was added to new centrifuge tubes and filled to the 35 mL line with ethanol. The mixture was centrifuged for 10 min at 10 000 rpm to precipitate nanoparticles. The supernatant was discarded, and the resulting nanoparticles were resuspended in 20 mL of hexanes. Approximately 4 mL of acetone was added to the centrifuge tube, and the mixture was centrifuged for 10 min at 10 500 rpm. The resulting supernatant was decanted into a new centrifuge and the resulting pellet was saved. Nanoparticles that crashed out first are the largest diameter nanoparticles (∼10 nm). To the supernatant 4 mL, acetone was added to the mixture and it was centrifuged for 10 min at 10 500 rpm. The process of saving the pellet of nanoparticles and adding acetone to the supernatant in a new centrifuge tube was repeated until the supernatant was clear. The size fractions of nanoparticles that resulted were 10, 7, 6, and 5 nm. The 6 nm nanoparticles were used for all experiments unless otherwise stated. The nanoparticles were washed two times with a 3:1 ratio of ethanol: hexane. The nanoparticles were suspended in 5 mL of hexanes for future use. Experiments using larger nanoparticles used the first fraction of nanoparticles from the size selection centrifugation.

Bulk Annealing of PdCu A1 Nanoparticles

As-synthesized PdCu A1 nanoparticles were evenly dispersed on a carbon support (Ketjenblack EC-600JD). The nanoparticles were massed and then resuspended in 2 mL of hexanes. The nanoparticles were then added dropwise to a slurry of the carbon support in 5 mL of acetone and 2.5 mL of hexanes. The mass between the nanoparticles and the carbon support was 1:1 for all experiments unless otherwise stated in the manuscript. Once the nanoparticles were added, the solution was sonicated for 1 h and then left to stir overnight. The resulting nanoparticles were dried, and the obtained solid was added to a dense alumina boat (AdValueTech). The boat was centered in a fused silica tube and placed in a tube furnace. The fused tube was purged with H_2/N_2 (4 v/v %) mixture for 30 min at room temperature, and then the sample was heated to the designated temperature at a ramp rate of 20 °C/min. The temperature and length of time were varied for different studies. For the temperature study, the samples were heated at 400, 450, 500, 550, and 600 °C for 3 h. For the time study, the samples were heated at 500 °C for 2, 6, and 8 h. The samples were cooled to room temperature and stored in a scintillation vial for further characterization. Temperature studies were also performed under Ar gas flow.

Characterization

All nanoparticles were characterized on JEOL JEM 1010 TEM, which operated at 80 keV, and images were collected with a ROM CCDE camera. TEM samples were dropcasted onto copper TEM grids after the sample was washed one time as previously described. Additional characterization with high-resolution transmission electron microscopy (HRTEM) and scanning transmission electron microscopy−energy-dispersive X-ray spectroscopy (STEM−EDS) was completed with JEOL JEM 3200FS operating at 300 keV, and images were taken with a Gatan 4k × 4k Ultrascan 4000 camera. The EDS mapping was obtained using Oxford Aztec dispersive X-ray system interfaced with JEOL JEM 3200FS. The samples were dropcasted onto gold TEM grids after five to six washes as previously described. Powder X-ray diffraction (XRD) patterns were collected on the Panalytical Empyrean instrument with Cu Kα radiation and an X'Celerator linear strip detector. The random alloy A1 PdCu reference is ICSD Collection Code 103084 and intermetallic B2 PdCu reference is ICSD Collection Code 181913. Rietveld refinements of the powder diffraction data were performed with GSAS-II software (Figures S1−

https://doi.org/10.1021/acsmaterialsau.1c00063
ACS Mater. Au 2022, 2, 143−153

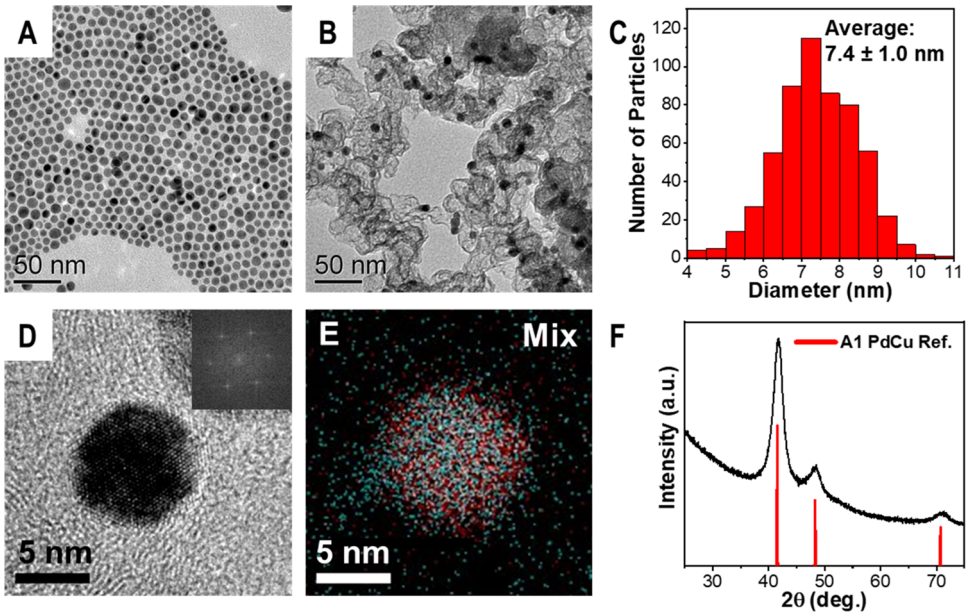

Figure 1. Characterization of random alloy PdCu nanoparticles. (A) TEM image of PdCu nanoparticles of A1 structure and (B) TEM image of A1 PdCu nanoparticles on a carbon support with (C) histogram of size distribution. (D) High-resolution TEM (HRTEM) image of an individual PdCu A1 nanoparticle with FFT inset. (E) Mixed mapping STEM−EDS with Cu shown in blue and Pd in red. (F) Powder XRD pattern of PdCu nanoparticles with a face-centered cubic random alloy configuration.

S5).[18] The background was described by a Chebyshev polynomial function, and peaks were described by the pseudo-Voigt profile function. The scale factor, cell parameters, profile parameters (W, U, V, and shape), and background points were generally refined. Crystallite domain size was also extracted from the powder diffraction data using Scherrer's equation (Tables S1−S4). The full width at half-maximum (FWHM) of the (111) reflection was determined in OriginPro via the multiple peak fit function. Scherrer's equation was used to determine the approximate crystallite domain size with the equation shown below.

$$\tau = \frac{\kappa\lambda}{\beta \cos\theta}$$

κ is the shape factor and 0.9 was used, which is typically used for spherical-shaped particles. λ is the X-ray wavelength and 1.5406 nm was used, which is the X-ray wavelength for a Cu-source. β is the FWHM and is converted to radians. θ is the Bragg angle of the peak, which is also converted to radians. The size of nanoparticles was measured from TEM images for nanoparticles with an automated MATLAB code and based on the contrast difference between nanoparticles and the background, and details can be found in the work reported by Harak et al.[19] Carbon-supported nanoparticles had to be manually measured in Fiji to determine their size.[20]

In Situ Heating TEM Experiments

They were conducted in a JEOL JEM 3200FS at 300 keV. The temperature was controlled using a Protochips Fusion Select heating holder with carbon-supported A1 PdCu nanoparticles (2:1 ratio of nanoparticles to carbon) dispersed in ethanol deposited onto E-FHDC-VO thermal E-chips. The E-FHDC-VO thermal E-chips have a carbon film with 2 micron holes as a sample support, which was found to be easier to perform HRTEM imaging than the continuous silicon nitride film. HRTEM images were collected in several locations at room temperature to find nanoparticles on their zone axis to make phase identification easiest. Images were acquired using a Gatan 4k × 4k Ultrascan 4000 camera with a 4096 × 4096 readout with a binning of 1 at a nominal magnification of 400k with a 1.0 s exposure time. Movies were not collected during the in situ heating TEM experiment due to the long period of the experiments (120 min). The electron dose was estimated based on the average number of electrons that interact with the CCD camera in the 1.0 s exposure time during image collection and dividing by the area of the image, resulting in an estimated average electron dose of 1710 $e^-/Å^2$. The Protochips Fusion Select holder was heated to 80 °C at a ramp rate of 40 °C/min and held at this temperature for 30−60 min to remove any leftover contamination. Then, the temperature was increased to 400 °C at a ramp rate of 40 °C/min, where HRTEM images were collected every 10 min for 120 min. The electron beam was blanked when not imaging during the 10 min increments. Fast Fourier transform (FFT) patterns were processed with Fiji from the collected HRTEM images.[20] The FFT patterns were compared to the reference FFT patterns generated from the reference cif files for A1 and B2 PdCu phases with SingleCrystal: a single-crystal diffraction program for Mac and Windows. CrystalMaker Software Ltd, Oxford, England (www.crystalmaker.com). Angles and distances between FFT spots were measured in Fiji and compared to the reference FFT patterns of A1 and B2 phases to determine the phase of the nanoparticle. The diameter of nanoparticles was also determined in Fiji.

RESULTS AND DISCUSSION

For these experiments, random alloy A1 PdCu nanoparticles were synthesized by a hot-injection method and deposited onto a carbon support in a 1:1 ratio of nanoparticles-to-carbon support (see the Experimental Methods section for full details). A1 PdCu nanoparticles were deposited onto a Ketjenblack carbon support as it is a common support in electrocatalytic applications of nanoparticles. The TEM images of as-prepared and supported nanoparticles are shown in Figure 1A,B, which have an average size of 7.4 ± 1.0 nm (Figure 1C). A high-resolution transmission electron microscopy (HRTEM) image in Figure 1D shows the lattice fringes and corresponding selected area fast Fourier transform (FFT) pattern of the HRTEM image (Figure 1D, inset), corresponding to the {110} planes of the random alloy A1 PdCu phase. Scanning transmission electron microscopy (STEM)/energy-dispersive X-ray spectroscopy (EDS) analysis, shown in Figure 1E, displays a uniform distribution of Pd and Cu at the single-particle level, with Pd represented in red and Cu in blue. The

https://doi.org/10.1021/acsmaterialsau.1c00063
ACS Mater. Au 2022, 2, 143−153

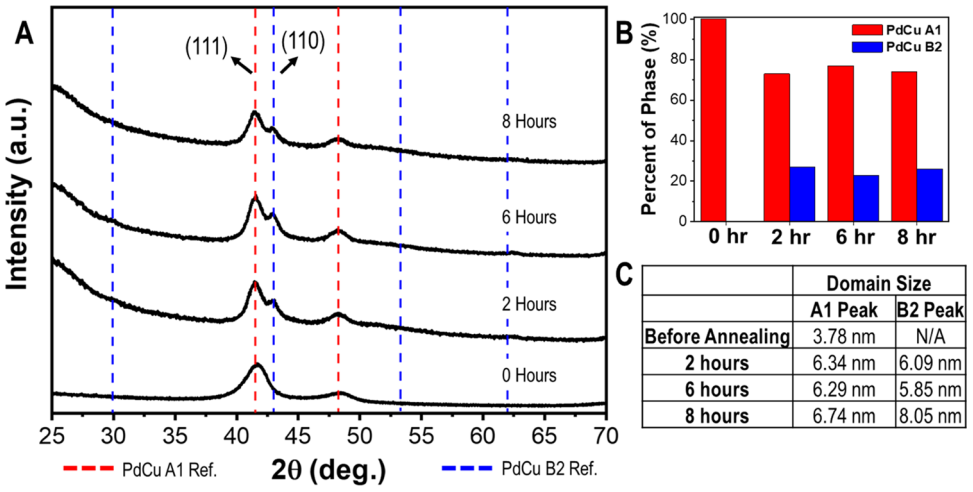

	Domain Size	
	A1 Peak	B2 Peak
Before Annealing	3.78 nm	N/A
2 hours	6.34 nm	6.09 nm
6 hours	6.29 nm	5.85 nm
8 hours	6.74 nm	8.05 nm

Figure 2. (A) XRD patterns from annealing carbon-supported A1 PdCu nanoparticles under H_2/N_2 gas flow for different lengths of time at 500 °C. (B) Graph of percent of A1 and B2 phases after heating carbon-supported A1 PdCu nanoparticles for the designated time, as determined from Rietveld refinement of XRD patterns. (C) Table reporting the crystallite domain size of A1 and B2 phases as determined by Scherrer's equation using the full width at half-maximum (FWHM) of the (111) reflection for the A1 phase and (110) reflection of the B2 phase.

powder XRD (Figure 1F) matches the reference pattern for the random alloy A1 phase of PdCu.

The carbon-supported random alloy PdCu nanoparticles were used in thermal annealing experiments to elucidate nanoscale processes involved in the disorder-to-order (A1 to B2 phase) transition. To begin, XRD was used to evaluate the extent of phase conversion and average crystallite size after annealing at various temperatures and lengths of time, with an objective being to identify the conditions that facilitate full conversion to the intermetallic phase. These XRD analyses were corroborated with TEM images of the samples after annealing and, together, helped to identify appropriate conditions for the in situ heating TEM experiments.

Specifically, carbon-supported random alloy PdCu nanoparticles, referred to as A1 PdCu/C throughout the rest of the paper, were annealed at 400, 450, 500, 550, and 600 °C under a flow of H_2/N_2 for 3 h to determine a temperature at which the disorder-to-order transition was sufficiently rapid. A flow of H_2/N_2 is commonly used during thermal annealing to achieve the intermetallic phase,[21,22] likely being adopted from early impregnation methods used to achieve and activate intermetallic nanoparticles for catalysis, where metal precursors were reduced at elevated temperatures under H_2/N_2 flow.[8] Figure S6 shows the TEM images of the resulting nanoparticles after annealing, displaying an overall increase in the average size of nanoparticles. Annealing at 500 °C resulted in the highest intensity (110) reflection for the B2 intermetallic phase (Figure S7). Rietveld refinements of powder XRD patterns were performed to determine the percent of A1 and B2 phases after annealing at the various temperatures (Figure S1). The highest percent of the B2 phase was observed at 500 °C (Figure S7B). This temperature was assigned as the disorder-to-order transition temperature for these annealing conditions.

A time study was then performed at 500 °C under a flow of H_2/N_2 to determine if complete conversion to the intermetallic phase could be achieved. TEM images were collected after annealing A1 PdCu/C nanoparticles for 2, 6, and 8 h (Figure S8), where the average sizes of nanoparticles were observed to increase after annealing from 6.6 ± 0.8 to 8.3 ± 1.8, 7.5 ± 1.4, and 8.2 ± 1.6 nm, respectively. The sizes of ∼100 nanoparticles were manually measured per sample as the carbon support inhibits automated analysis, which may account for some variation in sizes between annealing experiments particularly from orientation effects. Powder XRD patterns (Figure 2A) show that the relative intensity of the intermetallic B2 (110) reflection remained the same compared to the A1 random alloy (111) peak for each length of time. Rietveld's refinement of XRD patterns revealed that the percent of the B2 phase at each length of time was ∼25%, demonstrating that extended annealing times did not result in an increased amount of atomic ordering of nanoparticles (Figure 2B). The domain sizes of nanoparticles were extracted from XRD patterns using Scherrer's equation and the FWHM of A1 (111) and B2 (110) reflections. The calculated domain sizes for the A1 and B2 phases were approximately the same (Figure 2C).

Previous work from our group showed that, during the colloidal synthesis of PdCu nanoparticles, the intermetallic phase was not achieved until the nanoparticle size was increased by overgrowth at 270 °C.[13] When PdCu nanoparticles were supported on carbon, the intermetallic phase could be achieved; however, the average size of the nanoparticles was observed to increase, along with loss of monodispersity.[13] These observations suggest that there may be a size-dependent activation barrier to overcome to achieve ordering. Expanding on this hypothesis, we considered two strategies to deliberately increase the size of A1 PdCu/C nanoparticles and evaluated whether or not full conversion to the intermetallic phase could be achieved. In one approach, the number of nanoparticles on the carbon support was increased in an effort to increase the chances of nanoparticle coalescence, which would lead to a size increase. That is, A1 PdCu nanoparticles were deposited in a 2:1 ratio of nanoparticles-to-carbon support (Figure S9A). In the second approach, the size of initial nanoparticles was selected as 9 nm, compared to 6 nm in the initial screening experiments. Two experiments were conducted with 9 nm nanoparticles. The first held the number of nanoparticles on the support constant between the two sizes of initial nanoparticles (6 and 9 nm) (Figure S9B). The second decreased the loading of 9 nm nanoparticles on the carbon support, held at 1:1 ratio of nanoparticles to carbon, to minimize particle−particle interactions (Figure S9C).

https://doi.org/10.1021/acsmaterialsau.1c00063
ACS Mater. Au 2022, 2, 143−153

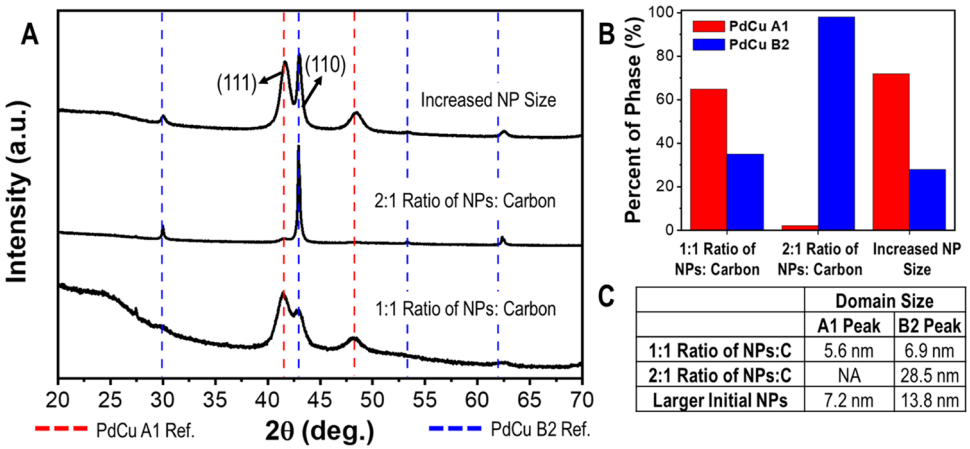

	Domain Size	
	A1 Peak	B2 Peak
1:1 Ratio of NPs:C	5.6 nm	6.9 nm
2:1 Ratio of NPs:C	NA	28.5 nm
Larger Initial NPs	7.2 nm	13.8 nm

Figure 3. (A) XRD patterns from the annealing experiment in which the number of nanoparticles on a carbon support was varied (1:1 and 2:1 ratio of nanoparticles: carbon) as well as from larger initial A1 nanoparticles (9 nm). (B) Graph of percent of A1 and B2 phases after heating carbon-supported A1 PdCu nanoparticles with deliberate size increase, as determined from Rietveld refinement of XRD patterns. (C) Table reporting the crystallite domain size of A1 and B2 phases as determined by Scherrer's equation using the FWHM of (111) for A1 and (110) for B2 reflection. All experiments were performed at 500 °C for 3 h under H_2/N_2 gas flow.

The A1 PdCu/C nanoparticles prepared by these three methods were annealed at 500 °C under H_2/N_2 flow for 3 h, and TEM images were collected of the resulting nanoparticles. In the case of the sample prepared with a 2:1 ratio of nanoparticles to carbon, the average size of the nanoparticles increased by ∼6 nm with a large standard deviation, indicating an increase in sample polydispersity (Figure S9D). In the case of the sample prepared with 9 nm nanoparticles at the same number of nanoparticles on the support as the initial 6 nm nanoparticle conditions, there was an increase in the average size by ∼4 nm, with a large standard deviation indicative of particle coalescence (Figure S9E). Adding 9 nm nanoparticles in a 1:1 mass ratio of nanoparticles to carbon reduced the number of particles on the support, which resulted in only a 1 nm increase in the average size of the nanoparticles with less polydispersity than the other samples (Figure S9F). While the intermetallic phase was achieved by maintaining the same number of 9 nm nanoparticles on the support as the 1:1 ratio of 6 nm nanoparticles to carbon (Figure S10), minimization of particle−particle interactions is important to make a more accurate determination of whether or not the size of initial nanoparticles influences the amount of atomic ordering. The 9 nm nanoparticles with a 1:1 ratio of nanoparticles-to-carbon support were used in further characterization methods as the reduction of the number of nanoparticles on carbon support allowed for direct analysis of the influence of the initial size of the nanoparticles.

Powder XRD patterns were collected for the samples after annealing (Figure 3A). The relative intensity of the (110) B2 reflection is greater than the intensity of the (111) A1 reflection for the sample with initially 9 nm nanoparticles. However, Rietveld refinement analysis (Figure S2) revealed the percent of the intermetallic phase was only 28%, showing that there was not a significant increase in the intermetallic phase compared to the initial sample (Figure 3B). Longer annealing times (8 h versus 3 h) did, however, increase the degree of ordering in the samples (Figures S11 and S12). The powder XRD pattern of the sample prepared with a 2:1 ratio of nanoparticles-to-carbon almost perfectly matched the B2 intermetallic reference pattern after annealing, indicating conversion to the intermetallic phase (Figure 3A). Rietveld's refinement of the XRD pattern revealed that there was 99% of the B2 phase (Figure 3B). The domain size calculated from the (110) B2 reflection is 28.5 nm, indicating that there is indeed an increase in the average size of nanoparticles after annealing (Figure 3C). This observation suggests that particle−particle interaction via coalescence may be important to induce the disorder-to-order transition.

Ex situ powder XRD and TEM analyses are valuable techniques to extract useful information about the disorder-to-order transition of PdCu nanoparticles; however, ex situ methods do not provide information on processes occurring at the nanoscale during annealing. In situ annealing TEM is a useful tool to observe morphological and crystal structure changes that occur during annealing. Huang and co-workers were able to observe the formation of intermetallic Pt−Sn nanoparticles with in situ heating electron microscopy, where the consecutive formation of ordered Pt_3Sn and PtSn phases were observed during the growth of intermetallic PtSn nanoparticles.[23] Before executing a full suite of in situ annealing TEM experiments, a series of control experiments were conducted. First, A1 PdCu/C nanoparticles were annealed under Ar flow to more closely simulate inert atmosphere conditions that would occur in the microscope as our heating holder did not allow for gas flow. A temperature study using a 1:1 ratio of nanoparticles to carbon revealed that the highest amount of the B2 phase occurred at 400 °C under Ar flow (Figures S13 and S14). This lower temperature was also beneficial for in situ heating TEM experiments as nanoparticles coalesced too quickly on the carbon support for useful imaging at 500 °C, particularly as nanoparticles did not remain on the zone axis for proper phase identification. Thus, conditions were selected that provided almost full conversion to the intermetallic phase but with a reduced rate of nanoparticle movement; A1 PdCu/C nanoparticles with a 2:1 ratio of nanoparticles-to-carbon support were heated at 400 °C for 120 min in a Protochips Fusion Select heating holder.

Additionally, an in situ heating TEM experiment was performed at these conditions, but the electron beam was blocked during the entire annealing period. TEM images were obtained at room temperature before annealing (Figure S15A) and after annealing at 400 °C for 120 min for the same region

https://doi.org/10.1021/acsmaterialsau.1c00063
ACS Mater. Au 2022, 2, 143−153

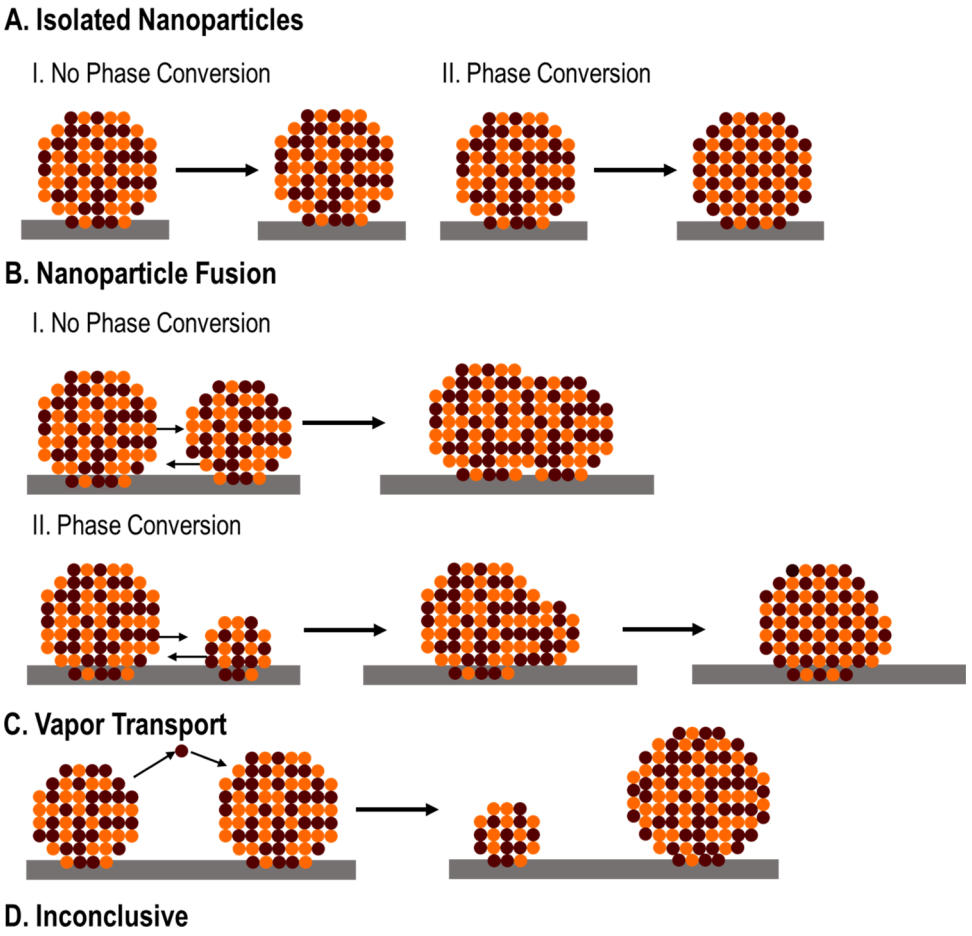

Figure 4. Schematic showing the various processes that were observed during in situ annealing TEM experiments where (A) isolated nanoparticles and (B) nanoparticles fused together were observed to undergo no phase change or a phase change. Evidence of (C) vapor transport was also observed, and some observed nanoparticle results could not be categorized, leading to an (D) inconclusive classification.

(Figure S15B) so those final products could both be compared to ex situ and in situ with imaging results. In this way, any effects from the environment of the heating holder and imaging conditions could be identified. Without in situ imaging but in situ heating, the morphology of nanoparticles was found to change to large aggregates on the carbon support (Figure S15B). Selected area electron diffraction (SAED) patterns were also collected of the area imaged before (Figure S15C) and after annealing (Figure S15D). The SAED pattern before annealing matches the reference pattern for the A1 phase, and the postannealing SAED pattern matches the reference pattern for the B2 phase and comprises of some A1 character, indicating that ordering occurs with heating in the TEM holder as expected from ex situ experiments. Looking more closely, an isolated nanoparticle of the A1 phase remained the A1 phase during annealing (Figure S16A and S16B) and coalescence of nanoparticles resulted in phase transformation from the A1 to the B2 phase (Figure S16C and S16D). As will be shown, similar processes are observed when the electron beam is introduced for imaging, suggesting that its effect is minimal. Nevertheless, the beam was blanked during periods when imaging was not occurring on account of the long annealing period (120 min) to ensure that the observed nanoscale processes were the result of annealing and not the electron beam.

That is, HRTEM images were collected every 10 min for the duration of the annealing experiments (see the Experimental Methods section for full details). Changes in morphology and crystal structure were monitored for 20 different nanoparticles during the annealing period, which were captured across multiple in situ heating TEM experiments. Figure 4 is a schematic depicting the five different processes observed during the in situ annealing experiments. Isolated nanoparticles remained in the random alloy A1 phase or transitioned to the intermetallic B2 phase. Nanoparticles fused with nearby nanoparticles and either remained in the random alloy A1 phase or converted to the intermetallic B2 phase. Finally, a reduction in nanoparticle size and their ultimate disappearance was observed, suggestive of vapor transport. In addition to these five processes, inconclusive classifications from four experiments were made due to nanoparticle orientation and imaging effects during the in situ heating TEM experiment.

Figure 5 shows an isolated nanoparticle that was observed to remain in the random alloy A1 phase during annealing at 400 °C. HRTEM images were collected at room temperature and every 10 min up to 90 min at 400 °C until the nanoparticle was no longer on the zone axis. The diameter of the nanoparticle was measured during annealing, and it is shown in the bottom right inset of the HRTEM images. The diameter of the nanoparticle decreased from 9.2 to 8.4 nm during annealing; however, the size decrease may be due to the shifting of the nanoparticle on the carbon support and not necessarily a change in the size of the nanoparticle. Selected area FFT patterns were obtained for the nanoparticle at different time

https://doi.org/10.1021/acsmaterialsau.1c00063
ACS Mater. Au 2022, 2, 143−153

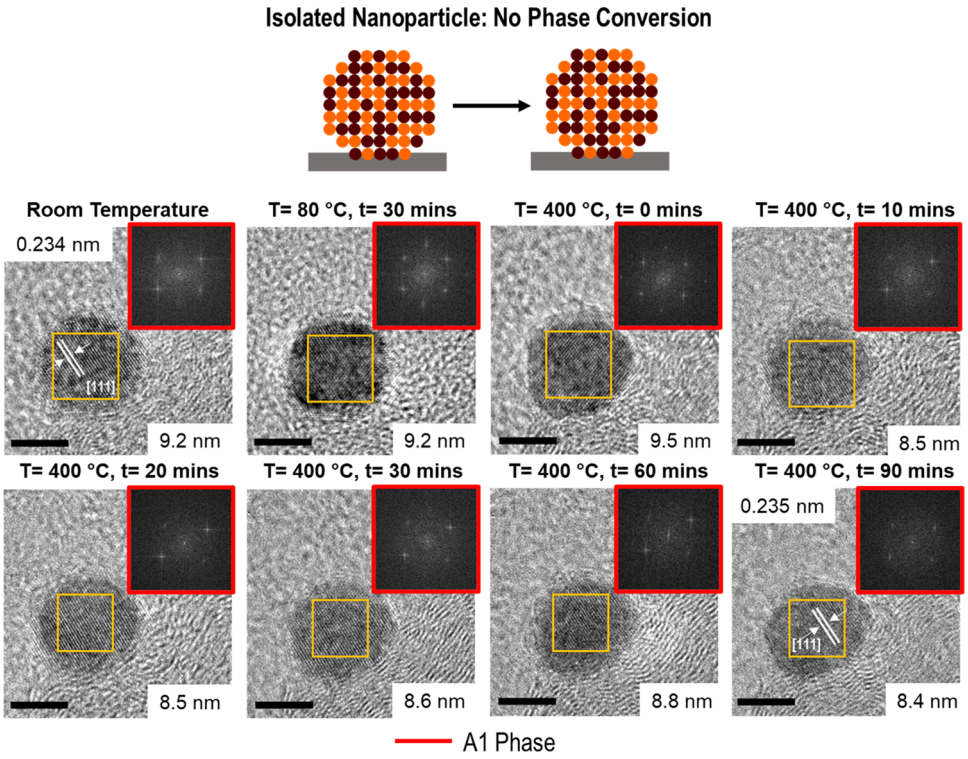

Figure 5. In situ annealing TEM experiment showing an isolated nanoparticle with no phase conversion. TEM images show the change in the nanoparticle during annealing at 400 °C for 90 min. The top right inset on TEM images is the corresponding selected area (yellow box) FFT with a red border showing that the phase was classified to be the A1 phase. The bottom right inset of TEM images is the measured diameter of the corresponding nanoparticle, and the top left inset is the interplanar distance measured at the beginning and end of the annealing period. All scale bars are 5 nm.

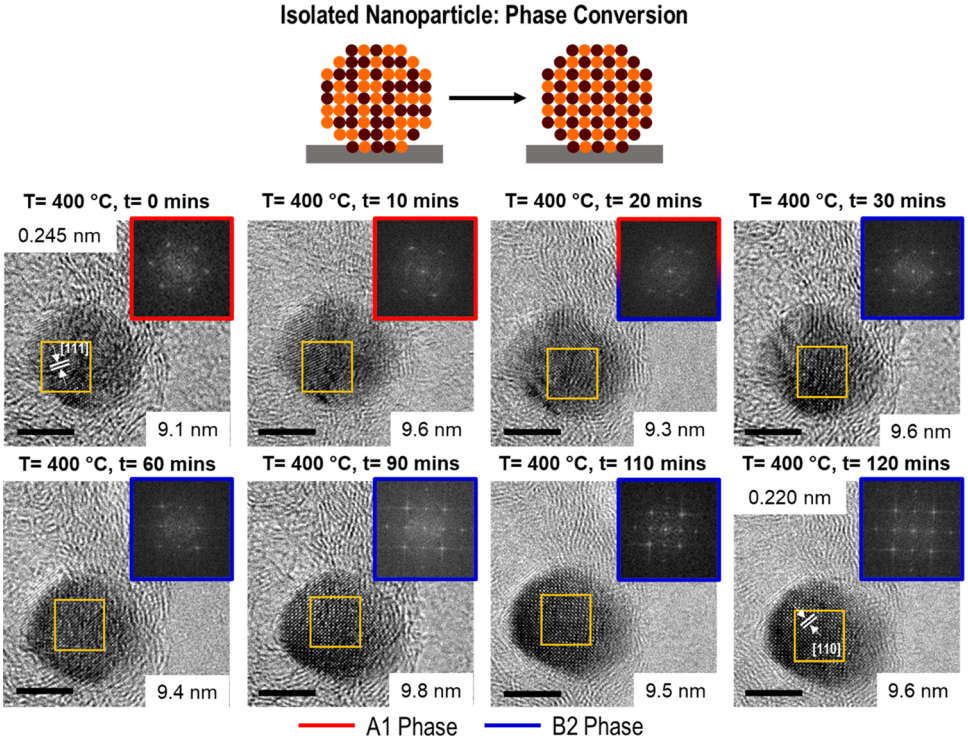

Figure 6. In situ TEM annealing experiment showing an isolated nanoparticle with a phase conversion. TEM images show the change in the nanoparticle during annealing at 400 °C for 120 min. The top right inset on TEM images is the corresponding selected area (yellow box) FFT with red border indicating the A1 phase identified and blue border indicating the B2 phase identified. The bottom right inset of TEM images is the measured diameter of the corresponding nanoparticle, and the top left inset is the interplanar distance measured at the beginning and the end of the annealing period. All scale bars are 5 nm.

https://doi.org/10.1021/acsmaterialsau.1c00063
ACS Mater. Au 2022, 2, 143−153

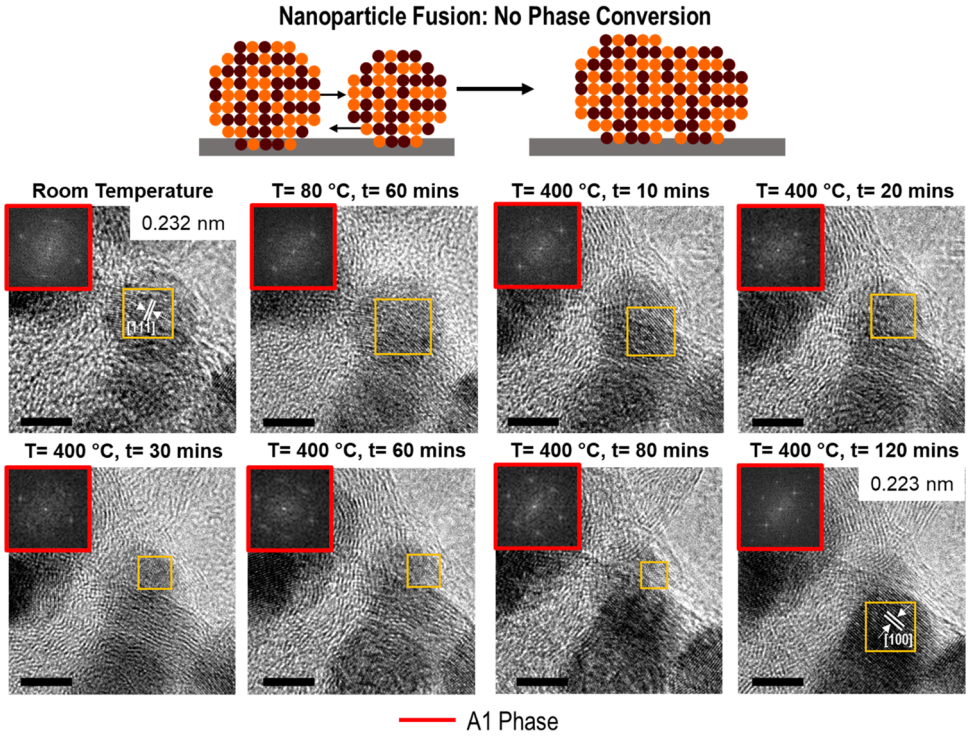

Figure 7. In situ annealing TEM experiment showing nanoparticle fusion with no phase conversion. TEM images show the change in the nanoparticle during annealing at 400 °C for 120 min. The top left inset on TEM images is the corresponding selected area (yellow box) FFT with a red border showing that the phase was classified to be the A1 phase. The top right inset is the interplanar distance measured at the beginning and the end of the annealing period. All scale bars are 5 nm.

points and analyzed to determine the phase of the nanoparticle via the method outlined in the Supporting Information and Figures S17−S19, where distances and angles between FFT spots were measured and compared to reference FFT patterns for the A1 and B2 phases of PdCu. Measuring the interplanar spacing of lattice fringes is another method toward phase identification; however, selected area FFT analysis is more reliable as larger regions of a nanoparticle can be analyzed rather than evaluating the change in space between two rows of atoms. Each FFT pattern for nanoparticle during annealing matched the <110> zone axis for the A1 phase. Out of 20 nanoparticles that were analyzed, 2 additional (3 total) isolated nanoparticles were observed to remain in the random alloy phase during annealing (Figures S20 and S21). Their diameters remained around 8−9 nm during annealing for the additional nanoparticles (Figures S20 and S21).

Not all isolated nanoparticles observed during annealing remained in the random alloy phase. Some isolated nanoparticles converted to the intermetallic phase, with one shown in Figure 6. Here, the diameter of the nanoparticle was observed to slightly increase from 9.1 to 9.6 nm after annealing for 120 min at 400 °C. However, again, variation in diameter could be due to the shifting of the nanoparticle on the carbon support and not a change in the size of the nanoparticle. The nanoparticle was identified to be the A1 phase at room temperature from the FFT pattern matching the reference pattern for the <110> zone axis of the A1 phase. The nanoparticle remained in the random alloy A1 phase up to 10 min at 400 °C. At 20 min, FFT spots that correspond to the A1 <110> zone axis and B2 <100> zone axis are observed, showing that there is conversion to the B2 phase. FFT patterns analyzed from 30 to 120 min correspond to the <100> zone axis of the B2 phase, indicating that the disorder-to-order transformation was achieved in this isolated nanoparticle. Five additional isolated nanoparticles (six in total) were observed to undergo the conversion to the intermetallic phase (Figures S22−S26) out of the 20 nanoparticles analyzed. The change in the diameter of these nanoparticles was minimal, remaining in a range of 8−9 nm.

Another event observed during annealing was a fusion of nanoparticles, where some nanoparticles remained in the random alloy A1 phase after coalescence with nearby nanoparticles. Figure 7 shows a nanoparticle fusion event that did not result in conversion to the intermetallic B2 phase after annealing at 400 °C for 120 min. Initially, at room temperature, the nanoparticle was observed to be 9 nm in diameter, where during annealing, the nanoparticle merged with a nearby nanoparticle domain. The FFT patterns of the initially observed nanoparticle were identified to correspond to the <110> zone axis of the A1 phase with no change observed throughout the annealing period as the nanoparticle merged with the neighboring nanoparticle domain. After 120 min of annealing, the originally observed nanoparticle had almost disappeared, and there is darker contrast of the neighboring nanoparticle domain observed. This observation suggests that there is fusion of the original nanoparticle with the neighboring nanoparticle domain. The phase of the nanoparticle domain after fusion still corresponds to the A1 phase, however, now the <100> zone axis. Only one additional fusion event was identified to remain in the A1 phase (Figure S27). Figure S27 shows the fusion of several particles where different domains of the merged nanoparticles were determined to remain in the A1 phase during the entirety of the annealing period. These fusion events that are observed to remain in the A1 phase may need a longer annealing period to achieve conversion to the intermetallic B2 phase.

https://doi.org/10.1021/acsmaterialsau.1c00063
ACS Mater. Au 2022, 2, 143−153

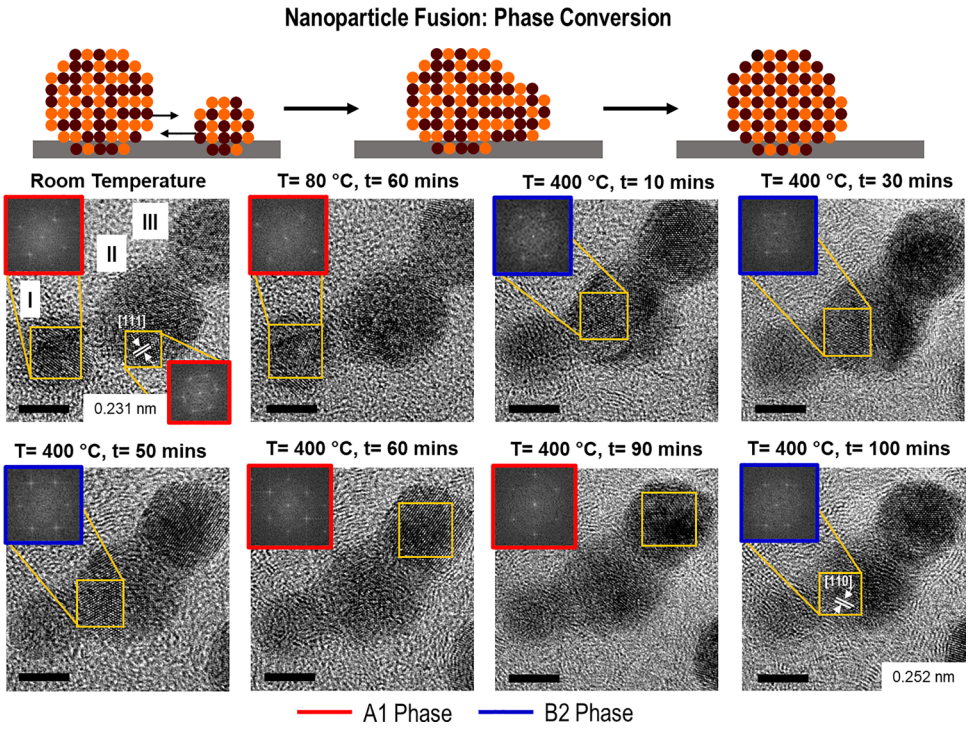

Figure 8. In situ TEM annealing experiment showing nanoparticle fusion with no phase conversion. TEM images show the change in the nanoparticle during annealing at 400 °C for 100 min. The top left inset on TEM images corresponds to the selected area FFT with a red border showing that the phase was classified to be the A1 phase. The bottom right inset is the interplanar distance measured at the beginning and the end of the annealing period. All scale bars are 5 nm.

In addition to nanoparticles remaining in the same phase during annealing when coalescing with neighboring nanoparticles, a few nanoparticles were observed to convert to the intermetallic B2 phase upon coalescence. Figure 8 shows a nanoparticle that converts to the intermetallic B2 phase when there is a fusion of a neighboring nanoparticle. Initially, three nanoparticles are in proximity with each other with FFT patterns of the three nanoparticles identified as the A1 phase (Figures 8 and S28). Nanoparticle I in Figure 8 is observed to merge with Nanoparticle II and after 100 min of annealing is reduced in size from 7.5 nm to approximately 5 nm. The contrast of Nanoparticle I was observed to become lighter during annealing, indicating the loss of metal. Interestingly, in parallel with fusion of Nanoparticle I with Nanoparticle II, there is a phase transformation of Nanoparticle II to the B2 phase. After annealing at 400 °C for 10 min, the FFT pattern of Nanoparticle II corresponds to the <111> zone axis of the B2 phase. Nanoparticle III also coalesces with Nanoparticle II; however, Nanoparticle III remains in the A1 phase during the annealing period and is observed to have minimal change in domain size (Figure S28). Two additional observed coalescence events led to conversion to the intermetallic B2 phase (Figures S29 and S30). Figure S29 shows two nanoparticles overlapping, and after 20 min of annealing, the domain of Nanoparticle II was classified as the B2 phase. Nanoparticle I was observed to remain in the A1 phase during the duration of annealing, yet the section of overlap between Nanoparticle I and II was determined to convert to the B2 phase. Figure S30 shows the transformation to the intermetallic B2 phase coincided with the coalescence of a smaller nanoparticle.

Another event observed during annealing of A1 nanoparticles was for isolated nanoparticles to decrease in size during the annealing time, suggestive of vapor transport. Figure S31 shows a nanoparticle that was classified as the A1 phase at room temperature, and upon annealing, the diameter decreased to the point that the nanoparticle had disappeared after annealing at 400 °C for 120 min. Figure S32 shows a similar occurrence; however, two nanoparticles were observed to reduce in diameter from 11 to 7.4 nm after annealing for 120 min. Leaching and/or dissolution is another possible route toward a decrease in the size of the nanoparticle, where individual metal atoms leave the surface of one nanoparticle. This process is typically accompanied by diffusion across the support and attachment to nearby particles.[24] However, in both examples, there were not any neighboring nanoparticles observed to increase in size during annealing. The observation suggests that vapor transport is occurring, where the path of atom migration to other particles or support out of view is through the vapor phase.[25] Due to the nature of the in situ TEM annealing experiment, the deposition of the vaporized material was not observed; however, this may be a possible route toward the size increase that is observed in bulk annealing experiments.

Other events were observed, but the classification of processes was challenging as particle orientations and imaging conditions did not facilitate phase identification. Figures S33–S35 show overlapping nanoparticles where phase identification and coalescence could not be confirmed. Figure S36 shows two nanoparticles sitting on top of each other with two domains of overlapping nanoparticles identified as the A1 phase at room temperature. Upon annealing, one domain of the nanoparticle is not on the zone axis and the phase cannot be identified, while the other domain remaining on the zone axis was observed to transform to the B2 phase after 70 min of annealing. This result was categorized as inconclusive due to

https://doi.org/10.1021/acsmaterialsau.1c00063
ACS Mater. Au 2022, 2, 143–153

the inability to assign a phase to the domain that did not remain on the zone axis, which could have remained A1 or transformed to the intermetallic phase. Also, it was unclear if nanoparticle fusion is what led to the phase transformation or the observed domain transformed on its own.

The diverse processes that are observed during in situ heating TEM show the origin of the heterogeneity that is observed after thermal annealing to achieve intermetallic nanoparticles. The in situ annealing TEM experiments show that some isolated nanoparticles can undergo the disorder-to-order transformation without growth. Moreover, coalescence events do not always result in the disorder-to-order transition in the observation period, which may reveal why long annealing times are needed to achieve full conversion to the intermetallic phase on the bulk scale. The in situ heating TEM experiments facilitate identification of processes occurring during annealing with nanoscale detail; however, caution is warranted when comparing these results to bulk measurements, such as powder XRD, as we have insufficient statistics to say what percentage of particles proceeds via one process versus another in their pathway to the intermetallic phase.

CONCLUSIONS

This work is a systematic investigation of nanoscale processes that occur during the disorder-to-order transformation of carbon-supported PdCu nanoparticles, with ex situ powder XRD and in situ heating TEM serving as useful tools for monitoring phase and morphology development. As was found, the number of nanoparticles on the carbon support had to be increased from initial studies to achieve nearly full conversion to the intermetallic phase (despite identical annealing conditions), showing the importance of coalescence events during heating. In situ heating TEM experiments at 400 °C revealed five different processes during the annealing of carbon-supported PdCu nanoparticles. Isolated nanoparticles either remained in the random alloy phase or were converted to the intermetallic phase. Nanoparticles that fused with nearby nanoparticles were observed to remain in the random alloy phase or convert to the intermetallic phase. Evidence of vapor transport was observed, as some nanoparticles were observed to slowly disappear during the annealing period. These varied nanoscale processes are responsible for the heterogeneity frequently found in intermetallic carbon-supported nanoparticle samples obtained by annealing. Overall, this work expands our understanding of the disorder-to-order transition of carbon-supported random alloy nanoparticles. In identifying nanoscale processes that occur during this process, these results now motivate the development of synthetic approaches that prevent particle−particle coalescence. Possible routes toward preventing particle−particle coalescence could be the use of sinter-resistant support materials and the physical confinement of the nanoparticle in an inorganic shell.[24] The interactions between metal nanoparticles with different types of supports have been extensively studied in the field of catalysis and ongoing work emphasizes developing strong adhesion of metal nanoparticles to supports to prevent particle−particle interactions.[24,26−31] Metal nanoparticles do not have strong adhesion to carbon-based supports and so it is important to expand investigations of this nature toward sinter-resistant supports.[32] Inspired by these studies, investigating the disorder-to-order phase transformation on different types of supports may induce this phase transformation under more mild conditions. Such advances are essential should monodisperse intermetallic nanoparticles be required.

ASSOCIATED CONTENT

Supporting Information

The Supporting Information is available free of charge at https://pubs.acs.org/doi/10.1021/acsmaterialsau.1c00063.

Materials and experimental methods, additional characterization (electron microscopy and XRD analysis), and control experiments (PDF)

AUTHOR INFORMATION

Corresponding Author

Sara E. Skrabalak − *Department of Chemistry, Indiana University, Bloomington, Indiana 47405, United States;* orcid.org/0000-0002-1873-100X; Email: sskrabal@indiana.edu

Authors

Hannah M. Ashberry − *Department of Chemistry, Indiana University, Bloomington, Indiana 47405, United States*

Xun Zhan − *Department of Chemistry, Indiana University, Bloomington, Indiana 47405, United States*

Complete contact information is available at: https://pubs.acs.org/10.1021/acsmaterialsau.1c00063

Author Contributions

The manuscript was written through contributions from all authors. H.M.A. executed the synthesis of PdCu nanoparticles, ex situ XRD analysis, and ex situ and in situ TEM analyses. X.Z. assisted in the setup of in situ annealing TEM experiments and analysis of FFT patterns. S.E.S. supervised the project and oversaw manuscript preparation. H.M.A. and S.E.S. are responsible for the project concept. All authors have approved the final version of the manuscript.

Notes

The authors declare no competing financial interest.

ACKNOWLEDGMENTS

S.E.S. and H.M.A. acknowledge financial support from Indiana University and U.S. DOE BES Award DE-SC0018961, both of which were used toward material synthesis, characterization, and catalytic evaluation. Access to the powder diffractometer was provided by NSF CHE CRIF 1048613. The authors also thank the IU Electron Microscopy Center and Nanoscale Characterization Facility for access to the necessary instrumentation.

REFERENCES

(1) Li, J.; Sun, S. Intermetallic Nanoparticles: Synthetic Control and Their Enhanced Electrocatalysis. *Acc. Chem. Res.* **2019**, *52*, 2015−2025.

(2) Xiao, W.; Lei, W.; Gong, M.; Xin, H. L.; Wang, D. Recent Advances of Structurally Ordered Intermetallic Nanoparticles for Electrocatalysis. *ACS Catal.* **2018**, *8*, 3237−3256.

(3) Yan, Y.; Du, J. S.; Gilroy, K. D.; Yang, D.; Xia, Y.; Zhang, H. Intermetallic Nanocrystals: Syntheses and Catalytic Applications. *Adv. Mater.* **2017**, *29*, No. 1605997.

(4) Zhou, M.; Li, C.; Fang, J. Noble-Metal Based Random Alloy and Intermetallic Nanocrystals: Syntheses and Applications. *Chem. Rev.* **2021**, *121*, 736−795.

(5) Gamler, J. T. L.; Ashberry, H. M.; Skrabalak, S. E.; Koczkur, K. M. Random Alloyed versus Intermetallic Nanoparticles: A Comparison of Electrocatalytic Performance. *Adv. Mater.* **2018**, *30*, No. 1801563.
(6) Rößner, L.; Armbrüster, M. Electrochemical Energy Conversion on Intermetallic Compounds: A Review. *ACS Catal.* **2019**, *9*, 2018−2062.
(7) Sun, S.; Murray, C. B.; Weller, D.; Folks, L.; Moser, A. Monodisperse FePt Nanoparticles and Ferromagnetic FePt Nanocrystal Superlattices. *Science* **2000**, *287*, 1989−1992.
(8) Wang, D.; Xin, H. L.; Hovden, R.; Wang, H.; Yu, Y.; Muller, D. A.; DiSalvo, F. J.; Abruña, H. D. Structurally Ordered Intermetallic Platinum−Cobalt Core−Shell Nanoparticles with Enhanced Activity and Stability as Oxygen Reduction Electrocatalysts. *Nat. Mater.* **2013**, *12*, 81−87.
(9) Qi, Z.; Pei, Y.; Goh, T. W.; Wang, Z.; Li, X.; Lowe, M.; Maligal-Ganesh, R. V.; Huang, W. Conversion of Confined Metal@ZIF-8 Structures to Intermetallic Nanoparticles Supported on Nitrogen-Doped Carbon for Electrocatalysis. *Nano Res.* **2018**, *11*, 3469−3479.
(10) Pei, Y.; Qi, Z.; Goh, T. W.; Wang, L.-L.; Maligal-Ganesh, R. V.; MacMurdo, H. L.; Zhang, S.; Xiao, C.; Li, X.; Tao, F.; Johnson, D. D.; Huang, W. Intermetallic Structures with Atomic Precision for Selective Hydrogenation of Nitroarenes. *J. Catal.* **2017**, *356*, 307−314.
(11) Xiong, Y.; Yang, Y.; Joress, H.; Padgett, E.; Gupta, U.; Yarlagadda, V.; Agyeman-Budu, D. N.; Huang, X.; Moylan, T. E.; Zeng, R.; Kongkanand, A.; Escobedo, F. A.; Brock, J. D.; DiSalvo, F. J.; Muller, D. A.; Abruña, H. D. Revealing the Atomic Ordering of Binary Intermetallics Using in Situ Heating Techniques at Multilength Scales. *Proc. Natl. Acad. Sci. U.S.A.* **2019**, *116*, 1974−1983.
(12) Yao, X.; Wei, Y.; Wang, Z.; Gan, L. Revealing the Role of Surface Composition on the Particle Mobility and Coalescence of Carbon-Supported Pt Alloy Fuel Cell Catalysts by In Situ Heating (S)TEM. *ACS Catal.* **2020**, *10*, 7381−7388.
(13) Wang, C.; Chen, D. P.; Sang, X.; Unocic, R. R.; Skrabalak, S. E. Size-Dependent Disorder−Order Transformation in the Synthesis of Monodisperse Intermetallic PdCu Nanocatalysts. *ACS Nano* **2016**, *10*, 6345−6353.
(14) Zhang, Q.; Li, F.; Lin, L.; Peng, J.; Zhang, W.; Chen, W.; Xiang, Q.; Shi, F.; Shang, W.; Tao, P.; Song, C.; Huang, R.; Zhu, H.; Deng, T.; Wu, J. Boosting Oxygen and Peroxide Reduction Reactions on PdCu Intermetallic Cubes. *ChemElectroChem* **2020**, *7*, 2614−2620.
(15) Marakatti, V. S.; Sarma, S. Ch.; Joseph, B.; Banerjee, D.; Peter, S. C. Synthetically Tuned Atomic Ordering in PdCu Nanoparticles with Enhanced Catalytic Activity toward Solvent-Free Benzylamine Oxidation. *ACS Appl. Mater. Interfaces* **2017**, *9*, 3602−3615.
(16) Wu, Z.-P.; Shan, S.; Xie, Z.-H.; Kang, N.; Park, K.; Hopkins, E.; Yan, S.; Sharma, A.; Luo, J.; Wang, J.; Petkov, V.; Wang, L.; Zhong, C.-J. Revealing the Role of Phase Structures of Bimetallic Nanocatalysts in the Oxygen Reduction Reaction. *ACS Catal.* **2018**, *8*, 11302−11313.
(17) Guo, Z.; Kang, X.; Zheng, X.; Huang, J.; Chen, S. PdCu Alloy Nanoparticles Supported on CeO2 Nanorods: Enhanced Electrocatalytic Activity by Synergy of Compressive Strain, PdO and Oxygen Vacancy. *J. Catal.* **2019**, *374*, 101−109.
(18) Toby, B. H.; Von Dreele, R. B. GSAS-II: The Genesis of a Modern Open-Source All-Purpose Crystallography Software Package. *J. Appl. Crystallogr.* **2003**, *46*, 544−549.
(19) Harak, E. W.; Koczkur, K. M.; Harak, D. W.; Patton, P.; Skrabalak, S. E. Designing Efficient Catalysts through Bimetallic Architecture: Rh@Pt Nanocubes as a Case Study. *ChemNanoMat* **2017**, *3*, 815−821.
(20) Schindelin, J.; Arganda-Carreras, I.; Frise, E.; Kaynig, V.; Longair, M.; Pietzsch, T.; Preibisch, S.; Rueden, C.; Saalfeld, S.; Schmid, B.; Tinevez, J.-Y.; White, D. J.; Hartenstein, V.; Eliceiri, K.; Tomancak, P.; Cardona, A. Fiji: An Open-Source Platform for Biological-Image Analysis. *Nat. Methods* **2012**, *9*, 676−682.
(21) Wang, Z.; Yao, X.; Kang, Y.; Miao, L.; Xia, D.; Gan, L. Structurally Ordered Low-Pt Intermetallic Electrocatalysts toward Durably High Oxygen Reduction Reaction Activity. *Adv. Funct. Mater.* **2019**, *29*, No. 1902987.
(22) Ma, S.; Sadakiyo, M.; Heima, M.; Luo, R.; Haasch, R. T.; Gold, J. I.; Yamauchi, M.; Kenis, P. J. A. Electroreduction of Carbon Dioxide to Hydrocarbons Using Bimetallic Cu-Pd Catalysts with Different Mixing Patterns. *J. Am. Chem. Soc.* **2017**, *139*, 47−50.
(23) Ma, T.; Wang, S.; Chen, M.; Maligal-Ganesh, R. V.; Wang, L.-L.; Johnson, D. D.; Kramer, M. J.; Huang, W.; Zhou, L. Toward Phase and Catalysis Control: Tracking the Formation of Intermetallic Nanoparticles at Atomic Scale. *Chem* **2019**, *5*, 1235−1247.
(24) Dai, Y.; Lu, P.; Cao, Z.; Campbell, C. T.; Xia, Y. The Physical Chemistry and Materials Science behind Sinter-Resistant Catalysts. *Chem. Soc. Rev.* **2018**, *47*, 4314−4331.
(25) Goula, G.; Botzolaki, G.; Osatiashtiani, A.; Parlett, C. M. A.; Kyriakou, G.; Lambert, R. M.; Yentekakis, I. V. Oxidative Thermal Sintering and Redispersion of Rh Nanoparticles on Supports with High Oxygen Ion Lability. *Catalysts* **2019**, *9*, No. 541.
(26) van Deelen, T. W.; Hernández Mejía, C.; de Jong, K. P. Control of Metal-Support Interactions in Heterogeneous Catalysts to Enhance Activity and Selectivity. *Nat. Catal.* **2019**, *2*, 955−970.
(27) Wang, L.; Wang, L.; Meng, X.; Xiao, F.-S. New Strategies for the Preparation of Sinter-Resistant Metal-Nanoparticle-Based Catalysts. *Adv. Mater.* **2019**, *31*, No. 1901905.
(28) Liu, J. Advanced Electron Microscopy of Metal−Support Interactions in Supported Metal Catalysts. *ChemCatChem* **2011**, *3*, 934−948.
(29) Ndolomingo, M. J.; Bingwa, N.; Meijboom, R. Review of Supported Metal Nanoparticles: Synthesis Methodologies, Advantages and Application as Catalysts. *J. Mater. Sci.* **2020**, *55*, 6195−6241.
(30) Campbell, C. T. The Energetics of Supported Metal Nanoparticles: Relationships to Sintering Rates and Catalytic Activity. *Acc. Chem. Res.* **2013**, *46*, 1712−1719.
(31) Campbell, C. T.; Sellers, J. R. V. Anchored Metal Nanoparticles: Effects of Support and Size on Their Energy, Sintering Resistance and Reactivity. *Faraday Discuss.* **2013**, *162*, 9−30.
(32) Takenaka, S.; Matsumori, H.; Nakagawa, K.; Matsune, H.; Tanabe, E.; Kishida, M. Improvement in the Durability of Pt Electrocatalysts by Coverage with Silica Layers. *J. Phys. Chem. C* **2007**, *111*, 15133−15136.

https://doi.org/10.1021/acsmaterialsau.1c00063
ACS Mater. Au 2022, 2, 143−153